Article

Red and Green Laser Powder Bed Fusion of Pure Copper in Combination with Chemical Post-Processing for RF Cavity Fabrication

Michael Mayerhofer [1,*], Stefan Brenner [2], Marcel Dickmann [1], Michael Doppler [3], Samira Gruber [4], Ricardo Helm [1], Elena Lopez [4], Verena Maier [5], Johannes Mitteneder [1], Carsten Neukirchen [6], Vesna Nedeljkovic-Groha [2], Bernd Reinarz [7], Michael Schuch [8], Lukas Stepien [4] and Günther Dollinger [1]

[1] Institute for Applied Physics and Measurement Technology, University of the Bundeswehr Munich, Werner-Heisenberg-Weg 39, 85577 Neubiberg, Germany
[2] Institute for Design and Production Engineering, University of the Bundeswehr Munich, Werner-Heisenberg-Weg 39, 85577 Neubiberg, Germany
[3] RENA Technologies Austria GmbH, Samuel-Morse-Straße 1, 2700 Wiener Neustadt, Austria
[4] Institute for Material and Beam Technology IWS, Fraunhofer Society, Winterbergstraße 28, 01277 Dresden, Germany
[5] Center for Applied Sciences and Tissue Engineering and Regenerative Medicine, Munich University of Applied Sciences, Lothstrase 34, 80335 Munich, Germany
[6] Institute of Chemical and Environmental Engineering, University of the Bundeswehr Munich, Werner-Heisenberg-Weg 39, 85577 Neubiberg, Germany
[7] Innovation Center Düsseldorf, EOS GmbH Electro Optical Systems, Fichtenstr. 53, 40233 Düsseldorf, Germany
[8] Bundeswehr Research Institute for Materials, Fuels and Lubricants (WIWeB), Institutsweg 1, 85435 Erding, Germany
* Correspondence: michael.mayerhofer@unibw.de

Abstract: Linear particle accelerators (Linacs) are primarily composed of radio frequency cavities (cavities). Compared to traditional manufacturing, Laser Powder Bed Fusion (L-PBF) holds the potential to fabricate cavities in a single piece, enhancing Linac performance and significantly reducing investment costs. However, the question of whether red or green laser PBF yields superior results for pure copper remains a subject of ongoing debate. Eight 4.2 GHz single-cell cavities (SCs) were manufactured from pure copper using both red and green PBF (SCs R and SCs G). Subsequently, the surface roughness of the SCs was reduced through a chemical post-processing method (Hirtisation) and annealed at 460 °C to maximize their quality factor (Q_0). The geometric accuracy of the printed SCs was evaluated using optical methods and resonant frequency (f_R) measurements. Surface conductivity was determined by measuring the quality factor (Q_0) of the SCs. Laser scanning microscopy was utilized for surface roughness characterization. The impact of annealing was quantified using Energy-Dispersive X-ray Spectroscopy and Electron Backscatter Diffraction to evaluate chemical surface properties and grain size. Both the SCs R and SCs G achieved the necessary geometric accuracy and thus f_R precision. The SCs R achieved a 95% Q_0 after a material removal of 40 μm. The SCs G achieved an approximately 80% Q_0 after maximum material removal of 160 μm. Annealing increased the Q_0 by an average of about 5%. The additive manufacturing process is at least equivalent to conventional manufacturing for producing cavities in the low-gradient range. The presented cavities justify the first high-gradient tests.

Keywords: additive manufacturing; RF cavity; 3D printing; selective laser melting; powder bed fusion; green laser powder bed fusion; red laser powder bed fusion; pure copper cavity; chemical post-processing

1. Introduction

More than 30,000 particle accelerators are used worldwide for a wide range of applications [1]. A large fraction of these accelerators are linear particle accelerators (Linacs). Some

of the most prominent fields of application include radiation therapy, the production of radioisotopes for medical diagnosis and therapy, food sterilization, the X-ray inspection of components, buildings, offshore containers, radiation hardening, the doping of microchips, material analysis, and fundamental research [1–5]. The vast majority of all Linacs are based on radio frequency (RF) cavities (hereafter referred to as cavities) [1,2]. Cavities are structures made of highly conductive materials (e.g., aluminum, copper, and superconductors) that enclose a vacuum volume. If an RF signal is coupled into the cavity whose frequency corresponds to the resonant frequency of the cavity (f_R), more energy is stored in the cavity than is dissipated by ohmic losses. The electric field (E-field) component, in the order of several hundred megavolts per meter, results in the cavity after many RF cycles have been used to accelerate the charged particles (e.g., electrons or protons) [2].

To enable efficient acceleration, the E-field must be concentrated on the beam axis, and the particles must be shielded from unwanted, decelerating field phases. For this purpose, among others, the internal geometry of most cavities is very complex, which is why they are conventionally manufactured in many individual parts. Subsequently, the single parts are joined through assembly methods such as brazing, electron beam welding, etc., to achieve vacuum tightness and optimal electric conductivity [6,7]. A series of consecutive precision steps incurring significant time and cost expenditures is necessary to manufacture complex cavity strutures. Considering the variability of cavity geometries and the fact that they can be different even in the same accelerator system, this manufacturing approach is almost impossible to automate. Thus, conventional cavity manufacturing constitutes a substantial portion of the capital investment costs associated with Linac systems [8–10]. Furthermore, it imposes limitations on cavity performance, serves as a source of defects during manufacturing, and obstructs the realization of new cavity designs [3,7].

Compared to conventional manufacturing processes, additive manufacturing (AM or colloquially known as 3D printing) allows the realization of highly complex geometries and thus customized and highly optimized components with improved performance. At the same time, material waste is minimized, and rapid prototyping is made possible [11–13]. The number of research projects that utilize these advantages to produce cavities is constantly increasing. Usually, normal conducting S band cavities, on which a large part of Linacs worldwide is based, are made of high-purity copper due to their exceptional electrical and thermal conductivity. Since their fabrication requires micron-level geometric precision, and sub-micron low surface roughness is beneficial to their performance, the laser powder bed fusion (L-PBF) process with subsequent surface post-processing is currently considered the best option for AM cavities [14,15].

During various research projects, several normal conducting copper cavity prototypes have been fully or partially manufactured with L-PBF. These included, among others, an interdigital H-mode cavity (433 MHz) [16,17], a high-frequency quadrupole (f_R = 750 MHz) [18,19], a quarter wave cavity resonator (f_R = 6 GHz) [20], a 3 GHz drift tube cavity [21,22] and single cells for Side-Coupled Cavity Linac Structures [23]. Through the various prototypes and other studies, it has been shown, among other things, that the following have been achieved:

1. The fabrication accuracy of L-PBF is sufficient to produce cavities with a resonant frequency lower than 4.2 GHz [23].
2. The manufactured cavities reach an inner pressure of less than $2 \cdot 10^{-7}$ mbar [22,24].
3. A quality factor Q_0 as in conventional manufacturing is achieved by electrochemical post-processing [23,25].
4. Manufacturing costs can be reduced by up to 70% using AM [21,22].

However, the evaluation of prototypes in high-gradient operation (at high coupled power), where surface defects can lead to voltage breakdowns that potentially damage the cavity, is still pending. Nevertheless, it has been shown that AM copper surfaces can withstand E-fields resulting from pulsed DC voltages up to approx. $40 \, \frac{\text{MV}}{\text{m}}$ [26].

Despite all the advantages that AM offers, there are also significant pitfalls, especially for new users or customers. DIN and ISO standards, which were developed for conven-

tional manufacturing, lose their relevance or are not applicable at all. Examples of this include dimensional parameters such as the arithmetic average of profile height deviations from the mean line R_a and the maximum peak to valley height of the roughness profile R_z for characterizing surface roughness [23,27]. The build quality is highly dependent on the printing parameters, part orientation, machine settings, and the diligence of the operators. Ultimately, the L-PBF systems from different manufacturers also exhibit significant variations. The choice of which machine to procure for a research project or to use for prototyping thus determines the achievable build quality, building size, and final cavity properties.

For high-performance components like cavities, it is imperative to optimize the manufacturing process for maximum performance. Especially in the case of pure copper cavities, a fundamental discussion arises in the community about whether an L-PBF system based on a red (1030 nm) or green (515 nm) wavelength laser should be used (hereinafter referred to as red and green laser). The absorption of the laser power for pure copper is at least a factor of 5 higher at 515 nm than at 1030 nm [28]. Since only one-fifth of the laser power is required to melt the material, L-PBF systems with green lasers could promise a more stable process with defined melt pools for dense material [29,30]. However, green laser systems have thus far exhibited significantly poorer focusing properties compared to red lasers. Machines equipped with red lasers thus have the possible potential to produce higher geometric accuracy and lower surface roughness [29–31].

In this work, we compare the printing quality of single-cavity (SC) prototypes ($f_R \approx 4.2$ GHz) manufactured using L-PBF systems with lasers in the green and red wavelength ranges (subsequently referred to as SC R or SC G). Four SCs were printed on both an EOS M290-1kW (SC R) and a TruPrint1000 Green Edition (SC G) to evaluate the geometric accuracy and electrical surface conductivity by measuring the f_R and their unloaded quality factor Q_0. In addition, the material density ρ, surface topology, and microstructure at the inner surfaces have been analyzed.

2. Materials and Methods

2.1. 4.2 GHz Cavity Prototype Design

L-PBF has the disadvantage that support structures are necessary to produce overhanging geometries (downskin sections, angle between geometry, and building platform $< 40°$) with a certain print quality (accuracy and roughness). These support structures provide temporary stability by anchoring the downskin sections to the build platform or previously printed parts of the geometry [32]. The removal of support structures from complex inner cavity geometries is possible, as we have already shown, but involves additional effort [25]. For this study, we therefore decided to adopt the self-supporting cavity geometry already presented in an earlier paper, in which downskin sections are reduced as far as possible [23]. Figure 1a shows the CAD drawing of the cavity in perspective. Figure 1b–d show the Y–X, Z–Y, and Z–X sections of the cavity geometry, respectively. The printing direction (building direction) corresponds to the z direction. In the following sections, we refer to the respective axes and planes.

The SCs are comparable to the unit cell cavities used in biperiodic side-coupled Linacs (SCCLs) [23]. However, unlike for their use in an SCCL, the geometry is provided with two coupling holes via which RF signals can be coupled in and out to feed or probe the RF field in the cavity. The electromagnetic behavior of the cavity was simulated with CST Microwave Studio$^®$ [33]. The E- and B-field distributions are shown in Figure 1e,f in the Z–X plane.

The simulated resonant frequency f_R of the cavity is 4260.1 MHz. The simulated unloaded quality factor Q_0 is 8100. The angle between building platform and downskin sections is always $\geq 45°$. As shown in [23], this cavity geometry can be manufactured using green laser L-PBF with the required accuracy for resonant frequencies below 4260 MHz. For the studies shown, the cavity geometry was also chosen because of its compact dimensions, which enable easy handling, as well as cost- and material-saving production.
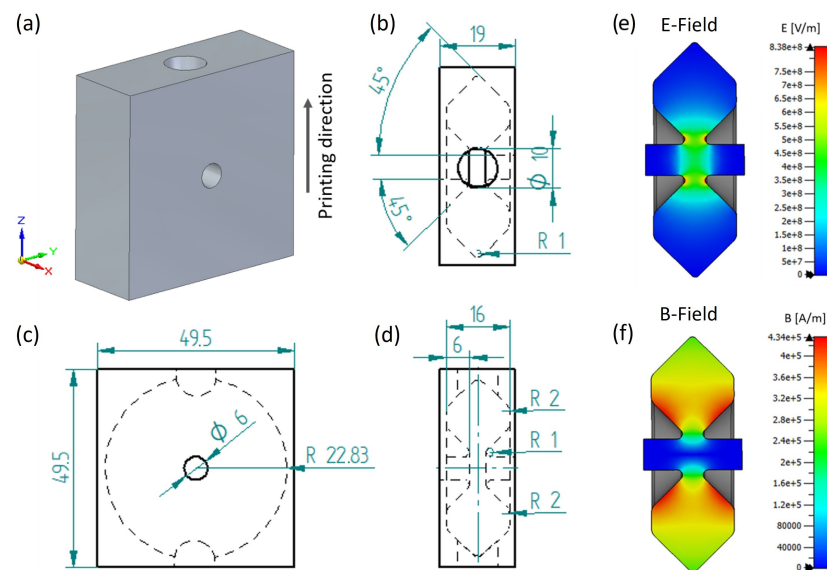
Figure 1. (**a**) CAD drawing of printed cavity in perspective. (**b–d**) show the Y–X, Z–Y, and Z–X sections of the cell geometry. (**e**) shows the E- and (**f**) the B-field distributions in the Z–X plane.

2.2. L-PBF Process

Green laser machine: We used a TruPrint1000 Green Edition equipped with a TruDisk1020 green laser ($\lambda = 515$ nm) and a maximum laser power of 0.5 kW of Fraunhofer IWS, Dresden, for manufacturing the cavities. The beam spot diameter at the laser focus point measures 210 µm. The pre-set pure copper manufacturing technological parameters and algorithms were used for the manufacturing process. The process parameters used have demonstrated relative densities exceeding 99.9% and electrical conductivity surpassing 100% IACS for pure copper by Gruber et al. [31]. PureCu® from m4p® was used as the raw material. The chemical composition corresponds to Cu (99.95%), Ag (<0.01%), Bi (<0.01%), Pb (<0.01%), O (0.023%), and a residue (0.01%). The particle size distribution corresponds to $d10 = 19$ µm, $d50 = 26$ µm, and $d90 = 36$ µm.

Red laser machine: We used an EOS M290-1kW equipped with a Yb fiberlaser ($\lambda = 1064$ nm) to manufacture the SC with red laser. The beam spot diameter at the laser focus point measures around 85 µm. The utilized process parameters are those developed by the manufacturer EOS, which have demonstrated relative densities exceeding 99.6% and electrical conductivity around 100% IACS for pure copper [34]. Again, not pure copper but EOS "CuCp" was used as the raw material.

2.3. Post-Processing

In line with prior studies, the process of Hirtisation® developed by RENA Technologies Austria [35] was used to diminish surface roughness post-printing [22]. Hirtisation® was also identified as the most promising post-processing method in a study on the post-processing of waveguide components [36]. Hirtisation® utilizes a combination of chemical/electrochemical processes to eliminate sintered-on particles or support structures. It also smoothens the component surface by selectively removing protruding portions of the surface profile more rapidly than recessed areas. In our case, the process employs Cu-Auxilex and Cu-Delevatex process media, also developed by RENA Technologies Austria GmbH [35]. In contrast to other processes for reducing the surface roughness of AM parts, only liquid media were used, which makes it possible to process small or difficult-to-access geometries. The desired material removal was determined by monitoring the material removal using a micrometer caliper on the outer geometries of the SCs. In earlier studies, it was noted that the gas bubbles produced by chemical processes, which always rise along the same paths in the process bath on the geometry surface, lead to an asymmetric material removal [23]. Asymmetric geometries lead to E-field peaks, which potentially promote

breakdown phenomena in high-gradient operation. It was therefore decided to divide the process time required for the desired material removal into four equal time periods, between which the orientation of the SCs in the process bath was changed by 90 degrees. The axis of rotation corresponds to the beam axis of the SCs.

The SCs were then annealed at a temperature of 460 °C in a Heraeus RE 1.1 vacuum tube furnace. The temperature was kept constant for 5 h, while the pressure in the vacuum tube remained between 10^{-7} and 10^{-6} mbar during the entire process.

2.4. RF Measurements

Resonant frequency (f_R) and Q factor (Q_0) were assessed through S_{21} measurements using a Siglent SNA5012A vector network analyzer (VNA) and two coupling loop probes (CLPs). Calibration of the VNA was performed at the top of the CLPs. Both CLPs were mounted on translation stages to attain optimal and consistently repeatable positioning accuracy.

Evaluation of dimensional accuracy: The geometric accuracy can be characterized by comparing the measured f_R with the simulated f_R. f_R is proportional to $\frac{1}{\sqrt{LC}}$, where L corresponds to the inductance, and C corresponds to the capacitance of the cavity. Since each geometrical deviation causes a change in L and C, the measurement of f_R cannot be used to infer a deviation at a specific location in the cavity.

An abrasion of a certain thickness in the cavity differently influences L and C of the hole structure. However, an abrasion of material at the drift tube nose has by far the largest impact on the resonance frequency f_R. For example, a material abrasion of 10 μm at the drift tube noses changes their distance by $\Delta d = 20$ μm and results in a frequency shift of $\Delta f_R = 4.2$ MHz according to a simulated dependency of $\frac{\Delta f_R}{\Delta d} = 0.21 \frac{\text{MHz}}{\text{μm}}$. In the following, the frequency shifts Δf_R are partially illustrated as a geometry deviation of the drift nose distance Δd.

Evaluation of electrical surface conductivity: The quality factor of a cavity can be expressed as $Q_0 = \frac{\omega_R W}{P}$. Here, P is the power loss per RF cycle with frequency $2\pi f_R = \omega_R$ in the cavity walls, and W is the energy stored in the cavity. Moreover, $Q_0 = G\sigma_0\delta$, where G depends only on the geometry of the cavity, and $\sigma_0\delta$ denotes the RF surface conductivity σ_{S0}. For annealed copper, the electric conductivity σ_0 corresponds to $58.1 \frac{\text{MS}}{\text{m}}$. The skin depth δ corresponds to $\approx$1 μm for an f_R of 4260.1 MHz. Assuming that G corresponds to that simulated by CST for the given geometry, an ideal $Q_{0\text{sim}} = 8100$ is calculated. Thus, a mean surface conductivity (σ_S) is extracted from a measured Q factor (Q_0) by $\sigma_S = \sigma_{S0} \cdot \frac{Q_0}{Q_{0\text{sim}}}$ [20].

2.5. Measurement on the Inner Cavity Surface

Following RF measurements, the SCs were cut in halves for inner surface evaluation through 3D optical scanning, roughness measurement, and microstructure analysis.

3D optical scanning: To create false color plots from the deviation of the printed geometry from the planned geometry (CAD file), thereby aiding in visualizing surface features, a Keyence VR-5000 system was employed utilizing structured light with 40× magnification and an automated stage. The measurement accuracy with image stitching is ±4 μm.

Surface roughness measurement: Surface roughness was characterized using the area root mean square average $S_{q\lambda}$, as introduced in [23]. This metric is similar to S_q defined in the ISO 25178 standard [37] but employs a different high-pass filter (λ_c filter) setting to eliminate surface waviness arising from the copper powder size. A Keyence VK-X3000 laser scanning microscope with a 20× extra-long working distance (ELWD) lens was used for surface characterization.

Data processing followed the method outlined in [23]. As depicted in Figure 2, roughness measurements were conducted at five locations on the inner cavity surface (compare Figure 1c). Red and green text indicated measurement points on the nose cone and cavity sidewall, respectively. Locations A and B corresponded to upskin and downskin surfaces defined from the printing direction, respectively, while positions C, D, and E represented

normal surfaces relative to the building platform. Each location encompassed an approximately 4 mm^2 area for evaluation.
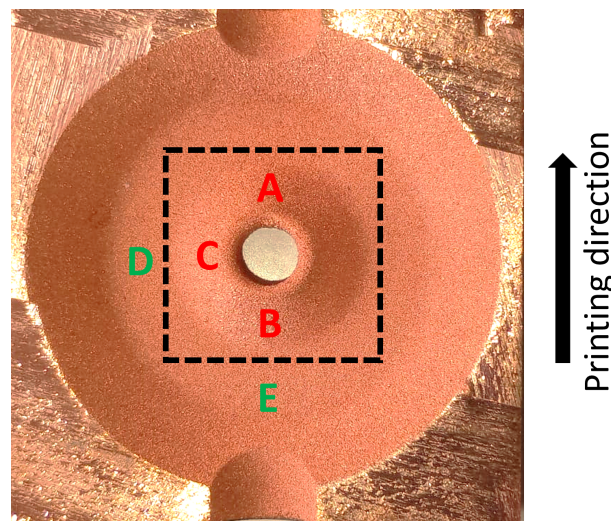

Figure 2. Locations for roughness measurement on the inner cavity surface.

The measured surface profiles underwent post-processing using Keyence software functions: *Noise removal* (set to "High") and *Missing data removal*. Following the method outlined in [23], the gradient model [38] was used to evaluate $\frac{\sigma_S}{\sigma_{S0}}$ based on surface roughness. For the AC surface resistance, surface changes that occur with a wavelength $\lambda \gg \delta$ can be considered as flat [38], where δ is the skin depth of copper. To consider only the surface variations under these conditions, a high-pass filter (λ_c-filter) was applied. We defined λ_c as the copper powder size $d50$, setting $\lambda_c = d50 = 26$ µm. To demonstrate the impact of λ_c onto the roughness analysis, the data were additionally evaluated with $\lambda_c = 14$ µm.

The lateral resolution of the Keyence VK-X3000 with the 20× ELWD lens is approximately 0.75 µm. After Hirtisation®, $S_{q\lambda}$ is expected to be considerably smaller than 1 µm. It is necessary to determine whether high-frequency surface variations exist that cannot be resolved using the optical method ($\lambda < 0.75$ µm) but are relevant for $S_{q\lambda}$.

To investigate this, the surfaces of two SCs, one produced with a red laser and the other with a green laser, were examined using an atomic force microscope (AFM). Six measurements were performed on SC R and SC G. Three of the six were each on a surface of the Z–Y and X–Y plane. Each measurement covered a 25 µm × 25 µm area with a 10 nm lateral resolution. For frequency-dependent analysis, $S_{q\lambda}$ was evaluated using cutoff wavelengths (λ_c) of 10 µm, 2 µm, and 0.5 µm. Figure 3 illustrates surface profiles of an SC produced with a red laser, which was post-processed with different $S_{q\lambda}$ values. Decreasing $S_{q\lambda}$ (from (a) to (d)) reveals roughness while retaining waviness.

Averaged over all 12 positions, $S_{q\lambda}$ values for different λ_c values were obtained: $S_{q\infty} = (158.0 \pm 70.8)$ nm, $S_{q10\mu m} = (73.7 \pm 28.6)$ nm, $S_{q2\mu m} = (15.5 \pm 4.0)$ nm, and $S_{q0.5\mu m} = (5.9 \pm 0.8)$ nm. Considering the lateral resolution of 0.75 µm of the Keyence VK-X3000, AFM measurements indicate the presence of high-frequency roughness $S_{q0.75\mu m}$ below approximately 10 nm. The overall roughness $S_{q\lambda}$ measured with the Keyence VK-X3000 after Hirtisation® is expected to be less than 300 nm (see Section 3.3). Since the contribution of high-frequency roughness (wavelengths smaller than 0.75 µm) to this overall roughness (wavelengths smaller than λ_c) is negligible, surface roughness in this work was determined using the optical method only.
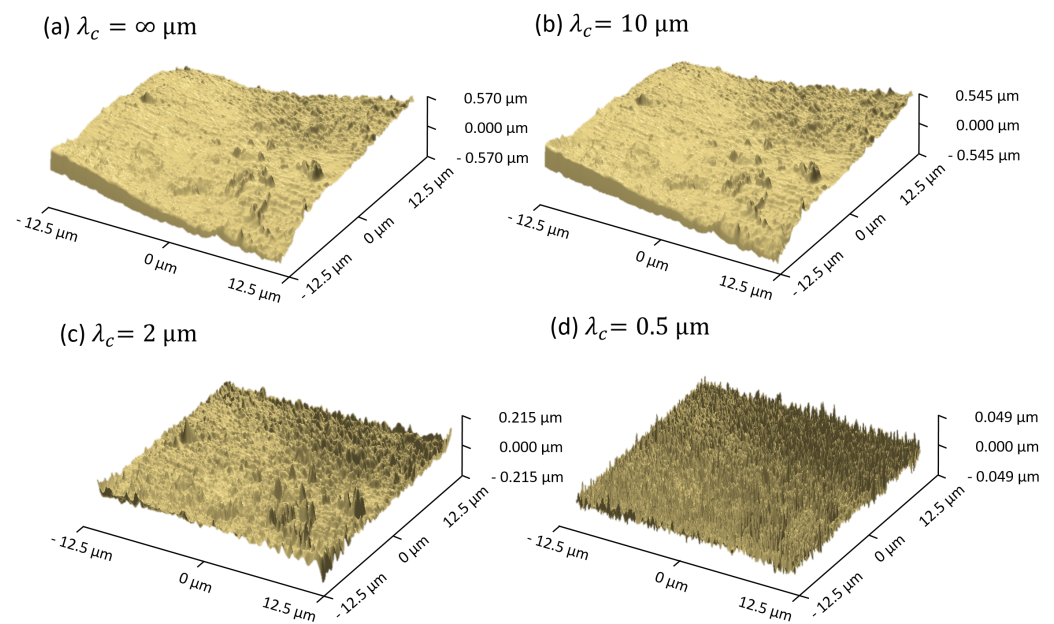
(a) $\lambda_c = \infty$ μm

0.570 μm
0.000 μm
- 0.570 μm

- 12.5 μm
0 μm
12.5 μm
- 12.5 μm
0 μm
12.5 μm

(b) λ_c = 10 μm

0.545 μm
0.000 μm
- 0.545 μm

- 12.5 μm
0 μm
12.5 μm
- 12.5 μm
0 μm
12.5 μm

(c) λ_c = 2 μm

0.215 μm
0.000 μm
- 0.215 μm

- 12.5 μm
0 μm
12.5 μm
- 12.5 μm
0 μm
12.5 μm

(d) λ_c = 0.5 μm

0.049 μm
0.000 μm
- 0.049 μm

- 12.5 μm
0 μm
12.5 μm
- 12.5 μm
0 μm
12.5 μm

Figure 3. Surface of the Z–Y plane the SC produced with red laser imaged with an atomic force microscope (AFM). A cutoff wavelengths filter (λ_c) of 10 μm (**b**), 2 μm (**c**), and 0.5 μm (**d**) was used to eliminate the waviness from the original image (**a**).

Material density, microstructure, and chemical analysis:

Despite achieving densities over 99.9% as standard with red and green laser L-PBF, this was confirmed through the examination of various micrographs from nose cone geometries manufactured with red and green lasers. Micrographs were captured for both X–Y and Z–Y plans of test prints of the nosecone geometries. The samples underwent embedding in resin and subsequent polishing. Density determination was conducted using images captured with the Keyence VK-X3000.

To analyze the microstructure, EBSD (Electron Backscatter Diffraction) measurements were performed on SC sample geometries produced with red and green lasers before and after annealing. Both the X–Y and Z–Y planes were examined for each SC sample geometry. Due to the skin effect, the microstructure of the inner cavity surface is of particular interest. The Z–Y plane was therefore examined at or as close as possible below the inner cavity surface, whereby, in contrast to the X-Y plane, three measurements were carried out on each sample. The copper samples were grinded with SiC paper with grid sizes of 600, 1200, 2500, and 4000. In the subsequent polishing steps, diamond pastes using water as lubricant with diamond particle sizes 3 μm and 1 μm was applied. To remove any surface deformation, samples were finally electrolytically polished with a LectroPol 5 device using Electrolyte D2 (both supplied by Struers, Copenhagen, Denmark). The best polishing results were obtained by cooling the electrolyte to approx. $-5°$ to $0°$ and applying a voltage of 25 V and a flow rate of 15 to 40 s. The EBSD investigation was performed with a Scanning Electron Microscope Tescan Mira 3 (Tescan, Brno, Crech Republic) equipped with an EBSD Detector (Oxford Nanosystems Ltd. Abingdon, UK). The acceleration voltage was set to 30 KV, and a step size of roughly 2.5 μm was used. For determination of the grain size, the results of typically 3 different areas with sizes of 2.5×1.9 mm were combined. To define a grain boundary, a misorientation angle of $5°$ was defined. Grains on the border of the area of interest and grains smaller than 10 pixels were excluded from the analysis. The equivalent circle diameter, the horizontal and vertical line intercept, and the misorientation angle distribution of the grain distributions were determined from the EBSD measurements.

Energy-dispersive X-ray spectroscopy (EDS) was used to investigate whether the manufacturing process, in particular post-processing, results in impurities on the surface. For this purpose, small samples were mechanically cut off the outsides of the SCs. For the

EDS spectra, 2048 × 1536 single measurements were summed up and carried out on an area of 3.61 mm × 2.71 mm. The measurement time per single measurement was 35 µs. The accelerator voltage was 5 kV.

3. Results

Figure 4 shows photographs of the final states of individual single cavities (SCs). The top row shows SCs produced using a red laser (R), while the bottom row shows those produced with a green laser (G). Each SC is labeled 1 through 4, corresponding to specific SCs within the respective laser types. SCs labeled 1 underwent no post-processing after printing. SCs labeled 2, 3, and 4 underwent material removal through Hirtisation®, with removal depths of 40 µm, 100 µm, and 160 µm, respectively. Figure 5 displays one half-cut each from the individual SCs in their final state, referencing Figure 4. Additionally, Figure 6 presents height profiles of the individual SC halves from Figure 5, captured using the Keyence VR-5000. It is crucial to note that the microscope's imaging accuracy is limited to areas with lateral extension relative to its objective. Angles close to 90° relative to the microscope stage, such as the inside of the drift tube or the cell interior's edge, may exhibit artifacts. Asymmetric features arising from the post-processing procedure are indicated by black and white arrows.
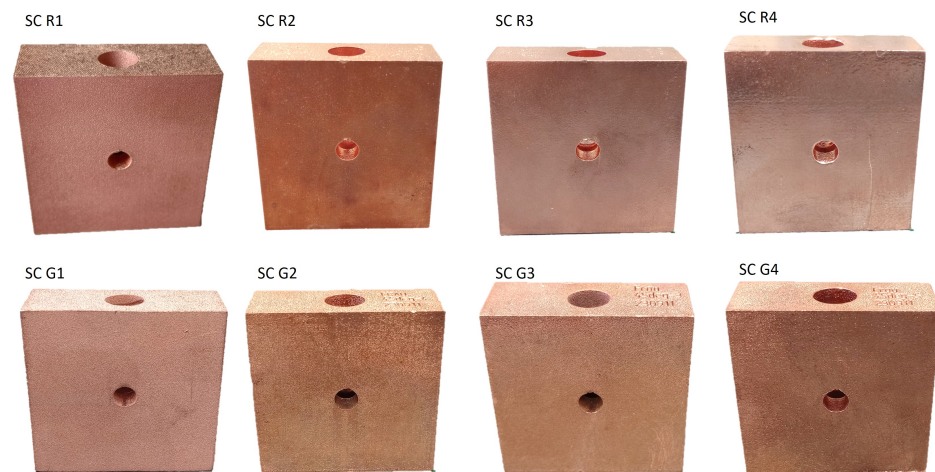

Figure 4. SC 1 is shown after printing. SC 2, SC 3, and SC 4 are shown after material removal of 40 µm, 100 µm, and 160 µm, respectively. SCs printed with green and red laser are indicated with G and R, respectively.
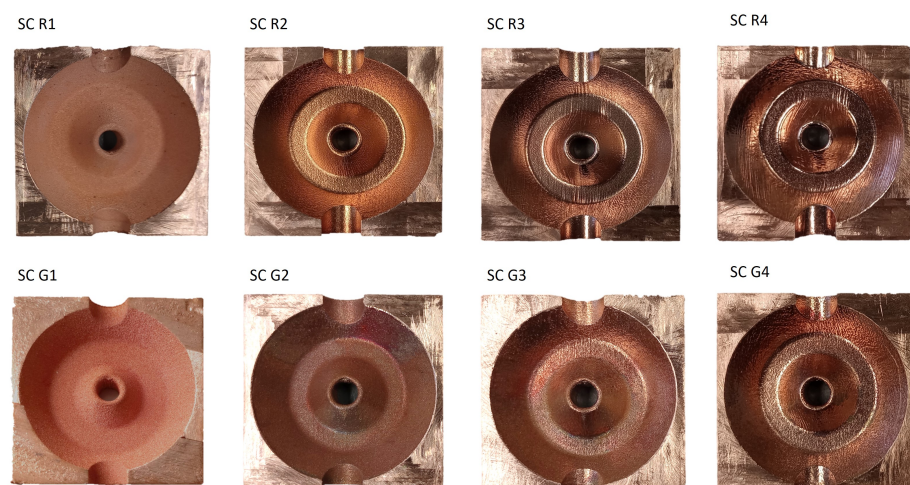

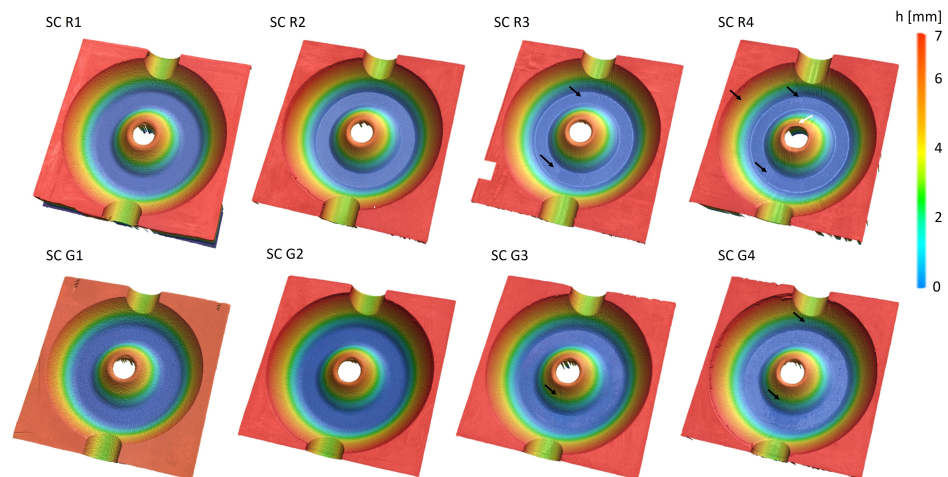**Figure 5.** One half of the individual SCs shown in Figure 4.

Figure 6. Height profile of the SC halves from Figure 5. Black and white arrows mark asymmetries caused by the post-processing process.

3.1. Density

Figure 7 depicts micrographs of the X–Y and Z–Y planes of a nose cone geometry printed using both red laser (R) and green laser (G). To generate high-resolution images, we stitched numerous individual images at high magnification, resulting in the contrast patterns observed in the images. Image analysis reveals densities of 99.68%, 99.63%, 99.76%, and 99.79% for R (a), R (b), G (a), and G (b), respectively. The densities for green laser (G) slightly lagged behind the potential densities achievable (>99.9% [31,34]). The small dark contrasts mark open-volume defects that are summed up to obtain their relative fraction of the whole volume.
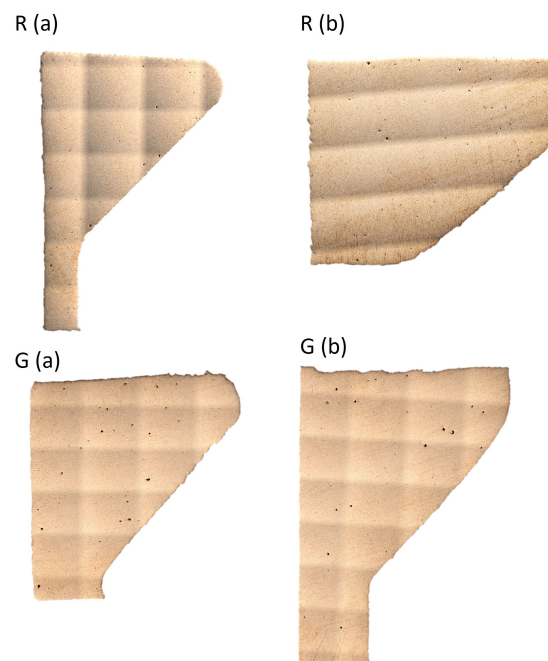

Figure 7. Micrographs of the nose cone geometry printed with red laser (R) and green laser (G). X–Y plane (**a**) and Z–Y plane (**b**) to the printing direction.

3.2. Resonance Frequency f_R

Table 1 presents the measured f_R values for the individual SCs post-printing. The measurement error of approximately 0.2 MHz for each value arose from (a) the positioning accuracy of the Coaxial Launch Probe (CLP) relative to its simulated position in CST and

(b) the accuracy of the VNA calibration. The mean resonance frequency $\bar{f}_R$ of the SC R and SC G deviated from the simulated f_R of 4260.1 MHz by 0.7 MHz and 3.9 MHz, respectively. The maximum deviation of the individual f_R values was 2.7 MHz and 5.0 MHz, respectively. The maximum deviation of the individual f_R from $\bar{f}_R$ corresponds to 1.1 MHz and 1.0 MHz, respectively.

Table 1. f_R of the SC numbers 1, 2, 3, and 4 manufactured with green and red laser L-PBF. The simulated f_R corresponds to 4260.1 MHz.

	f_R [MHz]				$\overline{f_R}$ [MHz]
Red laser	4260.5 ± 0.2	4260.8 ± 0.2	4259.3 ± 0.2	4262.8 ± 0.2	4260.8 ± 0.7
Green laser	4263.4 ± 0.2	4265.1 ± 0.2	4263.8 ± 0.2	4263.9 ± 0.2	4264.0 ± 0.4
SC	1	2	3	4	

Table 2 presents the measured f_R values for the individual SCs after Hirtisation® and annealing. SC R1 and SC G1 exhibited no significant change in the f_R within the measurement uncertainties compared to after printing. Hence, the influence of the annealing process on the geometry can be considered negligible.

Table 2. f_R of the SC numbers 1, 2, 3, and 4 manufactured with green and red laser L-PBF after Hirtisation® and annealing.

	f_R			
Red laser	4260.3 ± 0.2	4281.9 ± 0.2	4290.2 ± 0.2	4357.0 ± 0.2
Green laser	4263.4 ± 0.2	4301.2 ± 0.2	4317.4 ± 0.2	4328.5 ± 0.2
MR [µm]	0 (SC 1)	40 ± 15 (SC 2)	100 ± 15 (SC 3)	160 ± 15 (SC 4)

The measured f_R values for the individual SCs after printing and after Hirtisation® are summarized in Figure 8. SCs R are represented in red, while SCs G are depicted in green.
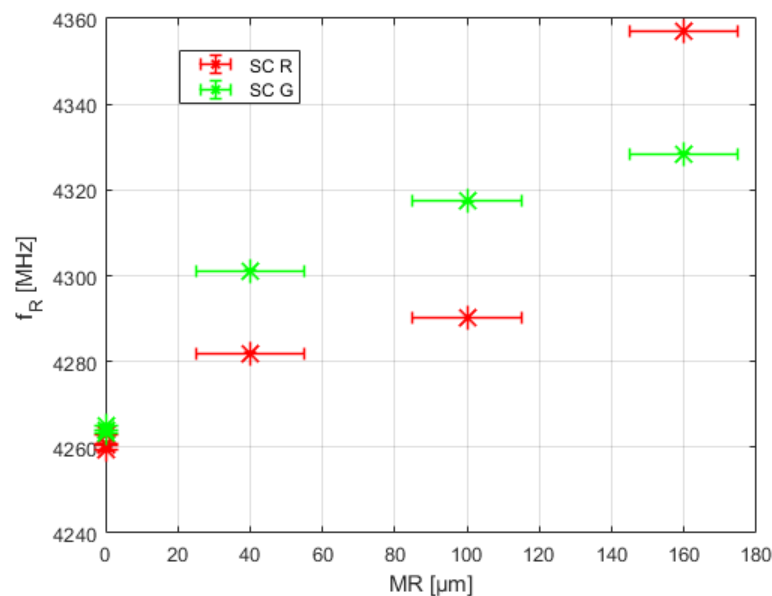

Figure 8. f_R after printing and after Hirtisation® of the individual SCs. SCs printed with red/green laser (SCs R and G) are marked in red/green color. MR refers to the material removal during Hirtisation.

3.3. Surface Roughness $S_{q\lambda}$

Table 3 provides a summary of the measured surface roughness $S_{q\lambda}$ at the designated locations indicated in Figure 2 for SC R1 and SC G1 as measured with the Keyence VK-

X3000 for a lateral upper cutoff wavelength of 26 μm ($S_{q26\mu m}$) and 14 μm ($S_{q14\mu m}$). SCs 2, 3, and 4 remained intact for post-processing and were consequently examined internally afterward. The average roughness $\overline{S}_{q\lambda}$ of SC G1 was approximately 43% higher than that of SC R1.

Table 3. $S_{q\lambda}$ at the specific locations (A, B, C, D, E) of SC 1 produced with green (G) and red lasers (R) after printing.

Location	A	B	C	D	E	
			$S_{q26\mu m}$ [μm]			$\overline{S}_{q26\mu m}$ [μm]
SC R1	2.85 ± 0.01	3.28 ± 0.01	3.32 ± 0.01	3.68 ± 0.01	3.13 ± 0.01	3.25 ± 0.15
SC G1	4.48 ± 0.01	4.20 ± 0.01	4.08 ± 0.01	5.24 ± 0.01	5.30 ± 0.01	4.66 ± 0.23
			$S_{q14\mu m}$ [μm]			$\overline{S}_{q14\mu m}$ [μm]
SC R1	1.93 ± 0.01	2.23 ± 0.01	1.95 ± 0.01	1.91 ± 0.01	1.80 ± 0.01	1.94 ± 0.15
SC G1	3.42 ± 0.01	3.34 ± 0.01	2.81 ± 0.01	4.39 ± 0.01	4.07 ± 0.01	3.61 ± 0.23

Table 4 provides a summary of the measured surface roughness $S_{q\lambda}$ at the designated locations marked in Figure 2 for all SCs. It is evident that the average roughness for both manufacturing methods decreased with increasing material removal. For SCs R, the most substantial reduction in $\overline{S}_{q\lambda}$ occurred with a removal of the first 40 μm. Conversely, for SCs G, a removal of at least 100 μm was necessary for a significant decrease in $\overline{S}_{q\lambda}$. Following a removal of 160 μm, SCs R exhibited an approximately 80% lower $\overline{S}_{q\lambda}$ compared to SCs G.

Table 4. $S_{q\lambda}$ at the specific locations (A, B, C, D, E) of all SCs produced with green (G) and red lasers (R) after printing, Hirtisation®, and annealing.

	SC G1	SC R1	SC G2	SC R2	SC G3	SC R3	SC G4	SC R4
MR [μm]	0		40		100		160	
$S_{q26\mu m}$ [μm] loc. A	4.48	2.85	3.24	0.57	1.97	0.57	0.51	0.45
$S_{q26\mu m}$ [μm] loc. B	4.20	3.28	1.12	0.85	0.61	0.72	0.98	0.54
$S_{q26\mu m}$ [μm] loc. C	4.08	3.32	5.35	0.76	1.70	0.52	0.66	0.47
$S_{q26\mu m}$ [μm] loc. D	5.24	3.68	4.47	0.60	0.84	0.55	0.94	0.39
$S_{q26\mu m}$ [μm] loc. E	5.30	3.13	5.29	0.54	0.83	0.54	0.97	0.40
$\overline{S}_{q26\mu m}$ [μm]	4.66	3.25	3.89	0.66	1.19	0.58	0.81	0.45
$S_{q14\mu m}$ [μm] loc. A	3.42	1.93	2.04	0.43	0.96	0.43	0.35	0.33
$S_{q14\mu m}$ [μm] loc. B	3.34	2.23	0.67	0.67	0.40	0.53	0.76	0.41
$S_{q14\mu m}$ [μm] loc. C	2.81	1.95	3.13	0.60	0.94	0.42	0.44	0.37
$S_{q14\mu m}$ [μm] loc. D	4.39	1.91	2.40	0.47	0.52	0.40	0.56	0.24
$S_{q14\mu m}$ [μm] loc. E	4.07	1.80	2.85	0.42	0.45	0.39	0.58	0.28
$\overline{S}_{q14\mu m}$ [μm]	3.61	1.94	2.22	0.52	0.65	0.43	0.53	0.33

3.4. Quality Factor Q_0

Table 5 displays the measured Q_0 values for the individual SCs post-printing. The average Q_0 of SCs R and SCs G corresponds to approximately 42% and 22% of the simulated $Q_0 = 8100$, respectively. Similar to f_R, the measurement error of the individual values arose from (a) the positioning accuracy of the Coaxial Launch Probe (CLP) relative to its simulated position in CST and (b) the accuracy of the VNA calibration.

Table 5. Q_0 of the cavity numbers 1, 2, 3, and 4 manufactured with green and red lasers after printing. The simulated Q_0 is 8100.

	Q_0				$\overline{Q_0}$
Red laser	3500 ± 100	3400 ± 100	3300 ± 100	3500 ± 100	3425 ± 70
Green laser	1800 ± 100	1700 ± 100	1700 ± 100	1800 ± 100	1750 ± 58
SC	1	2	3	4	

Table 6 shows the measured Q_0 values for the individual SCs after Hirtisation®. For SC R2, SC R3, and SC R4, the Q_0 increased by 126%, 133%, and 140% compared to after printing SC R1 (see Table 5). For SC G2, SC G3, and SC G4, the Q_0 increased by 100%, 241%, and 283% compared to SC G1 after printing.

Table 6. Q_0 of the cavity numbers 1, 2, 3, and 4 manufactured with green and red lasers. Cavity numbers 2, 3, and 4 after Hirtisation®.

	Q_0			
Red laser	3500 ± 100	7700 ± 100	7700 ± 100	8400 ± 100
Green laser	1800 ± 100	3400 ± 100	5800 ± 100	6900 ± 100
MR [µm]	0 (SC 1)	40 ± 15 (SC 2)	100 ± 15 (SC 3)	160 ± 15 (SC 4)

Table 7 presents the measured Q_0 values for the individual SCs after Hirtisation® and annealing. SC R1 exhibited a notable increase in the Q_0 of approximately 60%. However, the Q_0 values for SC R2 to SC R4 only showed marginal increases of approximately 3% to 4% compared to those shown in Table 6. Conversely, SC G1 showed no significant increase in the Q_0 due to annealing. SC G2 experienced an increase of approximately 11%, while SC G3 and SC G4 showed increases of around 5%.

Table 7. Q_0 of the cavity numbers 1, 2, 3, and 4 manufactured with green and red lasers after printing, Hirtisation®, and annealing.

	Q_0			
Red laser	4100 ± 100	8000 ± 100	7900 ± 100	8700 ± 100
Green laser	1800 ± 100	3800 ± 100	6100 ± 100	7200 ± 100
MR [µm]	0 (SC 1)	40 ± 15 (SC 2)	100 ± 15 (SC 3)	160 ± 15 (SC 4)

The measured Q_0 values of the individual SCs after printing, Hirtisation®, and annealing are summarized in Figure 9. SCs R are represented in red, while SCs G are depicted in green. Crosses indicate the SC before, and circles denote the SC after annealing.

Figure 10 displays the measured Q_0 of the individual SCs after printing, Hirtisation®, and annealing, which are plotted against $S_{q\lambda}$. Dots with crosses represent the values corrected with $\lambda = 26$ µm and $\lambda = 14$ µm—the "cutoff" filter. The black dashed line represents the expected Q_0 values according to the gradient model. With a cutoff wavelength of $S_{q\lambda} = 26$ µm, neither the measured Q_0 of the SC R nor that of the SC G corresponds to the gradient model. Looking at the roughness, the deviation is in the order of magnitude of the measured value itself. For $S_{q\lambda} = 14$ µm, only SC G2, SC G3, and SC G4 correspond to the gradient model within the scope of the measurement uncertainty. All other SCs showed deviations from the model, but these were significantly smaller compared to the deviations of $S_{q\lambda} = 26$ µm.
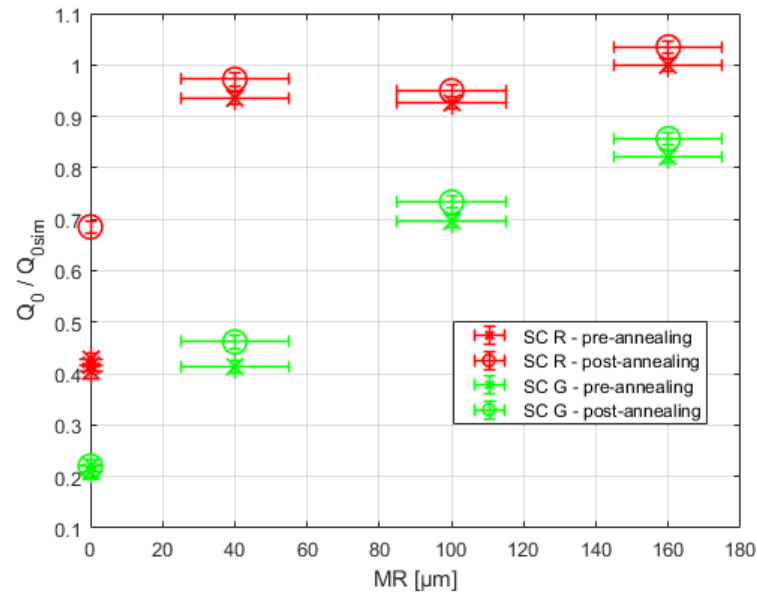
Figure 9. Q_0 of the SC printed with red (red color) and green laser (green color). Values after Hirtisation® are marked with a cross, and values after annealing are marked with a circle.
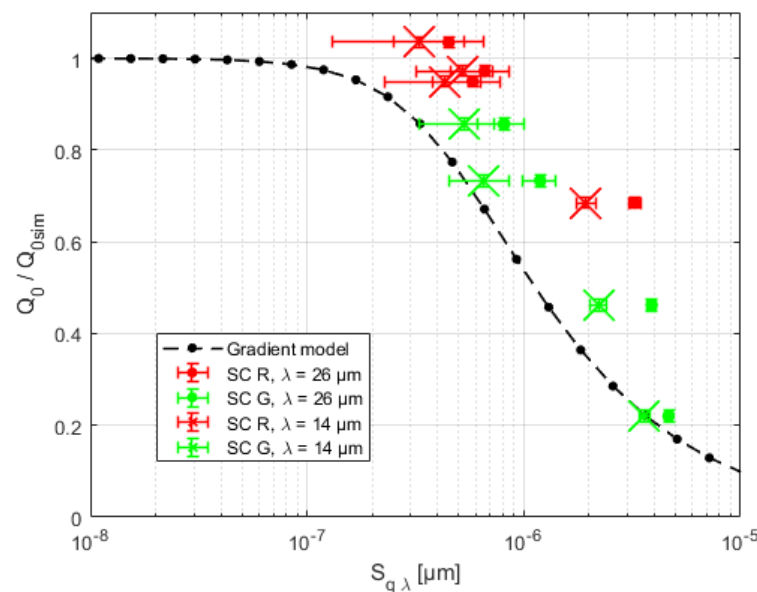

Figure 10. Q_0 of the SC printed with red (red color) and green laser (green color) after Hirtisation® and annealing. Dots and crosses represent the values corrected with the 26 μm and 14 μm "cutoff" filter. The black dashed line represents the Q_0 values as expected according to the gradient model.

3.5. Impact of Annealing

The annealing process resulted in a white coating forming on the quartz tube of the vacuum furnace, likely attributed to outgassing from the SCs. Consequently, we conducted a more detailed analysis to determine which process was responsible for the increase in the unloaded quality factor.

Energy-dispersive X-ray spectroscopy (EDS) revealed the coating in the quartz tube of the vacuum furnace as copper(I)-chloride (CuCl). Figure 11a displays an EDS map of the sample, with the sample carrier depicted in blue (carbon). To identify the source of CuCl, sections of the SCs were analyzed post-additive manufacturing (Figure 11b), post-Hirtisation® (Figure 11d), and post-annealing (Figure 11e). Figure 11c shows a section of b

enlarged. Figure 11f presents the EDS spectra after printing, Hirtisation®, and annealing, as well as the EDS spectra of CuCl. Spectra normalized to 1 with respect to the copper peak are shown. Figure 11g shows the chlorine peaks in detail. The chlorine content increased post-Hirtisation® from 0.3% up to 0.8% but decreased significantly to 0.1% after annealing. However, EDS analysis has limitations when analyzing thin layers. Due to the energy requirements for chlorine excitation, an accelerator voltage of 5 kV was used. We simulated that the average penetration depth of 5 keV photons in copper and chloride was approx. 50 nm. If the layers to be analyzed are significantly thinner, as we assumed in the case of CuCl, the determination of CuCl concentrations will be effected. Nevertheless, the post-processing can be evaluated based on the relative change.

In addition, aluminum oxide (AlO) was found on the sample after printing (see, Figure 11b,c), which resulted in the high Al peak in the spectrum. The AlO was removed by the Hirtisation® process (see Figure 11d), causing the Al peak in the spectrum to disappear and the O peak to decrease. It is also noticeable that the oxygen content dropped again after annealing. This could be due to CO_2 or H_2O dissolving from the surface at high temperatures. It is not clear where the AlO came from. Contamination of the powder can be ruled out, as the AlO vanished after Hirtisation® was applied. We therefore tend to assume contamination with Al during the preparation of the sample (during cutting or similar). This thesis is also supported by the fact that aluminum (660 °C) has a melting temperature that is below that of copper (1085 °C). However, the impurity appears to be local and not fused with the copper.
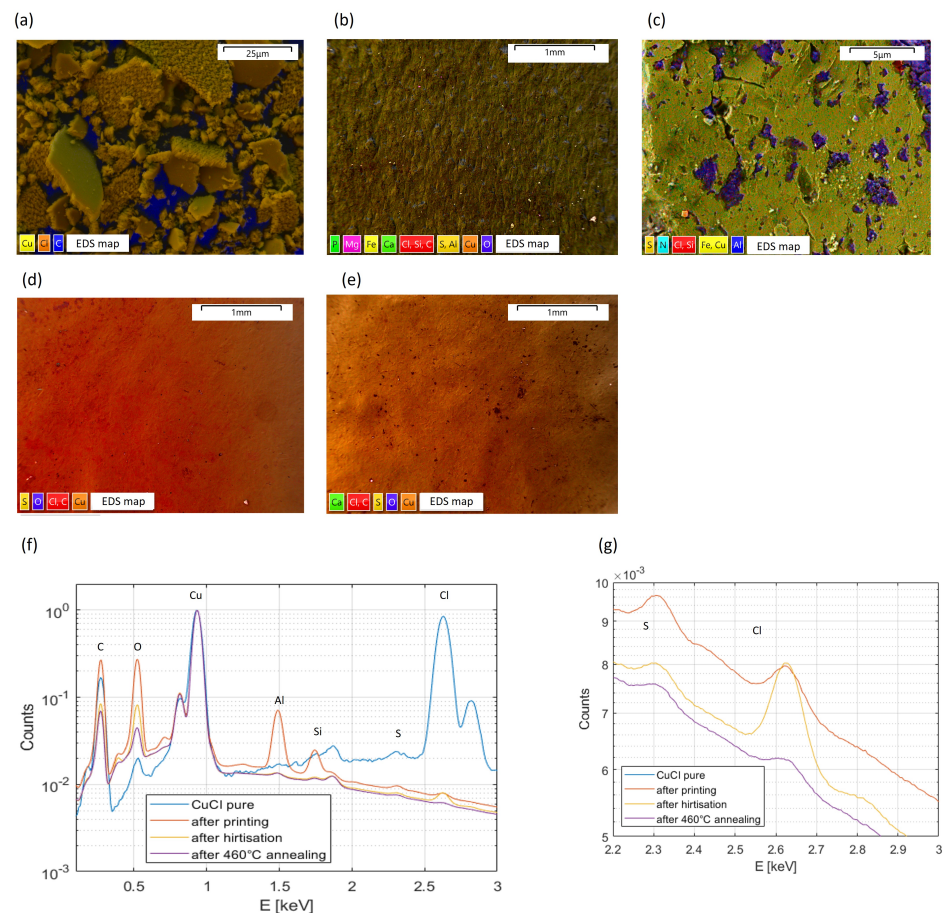

Figure 11. (**a,b,d,e**): EDS map of the sample taken from the quartz tube coating, after printing, after Hiritisation®, and after annealing. (**c**) Magnification of an area of (**b**). (**f**) EDS spectra of CuCl and copper samples after printing, after Hirtisation®, and after annealing. Normalized to 1 with respect to the copper peak. (**g**) EDS spectra in detail around the element Cl.
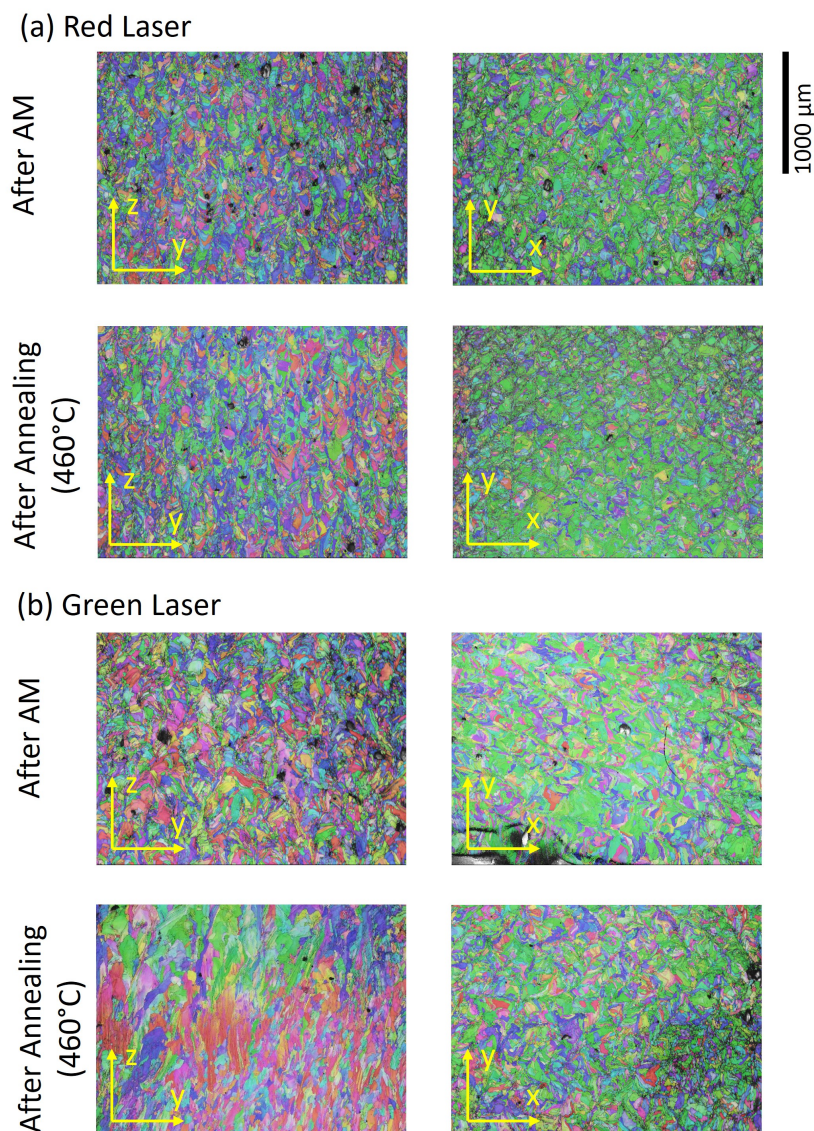
Figure 12 shows exemplary electron backscatter diffraction (EBSD) maps of sample geometries produced with red (a) and green (b) lasers before and after annealing. The first column displays micrographs parallel to the building direction (Z–Y plane), while the second column shows the X–Y plane. The grain orientation preferably corresponds to an orientation of [100] or [101] perpendicular to the building direction, whereby the preferred orientations depend on the cooling rate [39] and the melt pool geometry [40–42]. Independent of the production process, a significant spatial variation of the microstructure was found in every sample. However, a careful statistical analysis shows that the grain sizes were in the range of 10 μm and 30 μm, with virtually no effect on the annealing treatment and production process. The calculated equivalent circle diameters, as well as the horizontal and vertical line segments, are summarized in Table 8. The spatial variations of the texture on the sample were therefore larger than the variations between different production processes.

Figure 12. Electron backscatter diffraction (EBSD) maps of samples produced with red (**a**) and green (**b**) lasers before and after annealing (X–Y plane and X–Y plane).

Table 8. Equivalent circle diameters (ECDs), horizontal line intercept (HLI), and vertical line intercept (VLI) of the EBSD maps shown in Figure 12.

Laser	State	Plane	ECD [μm]	HLI [μm]	VLI [μm]
Red	After AM	Z-Y	21 ± 17	14 ± 12	23 ± 24
		X-Y	17 ± 17	13 ± 11	17 ± 14
	After Annealing	Z-Y	18 ± 11	11 ± 10	15 ± 14
		X-Y	14 ± 7	14 ± 12	15 ± 11
Green	After AM	Z-Y	21 ± 16	16 ± 15	22 ± 20
		X-Y	15 ± 8	13 ± 14	14 ± 14
	After Annealing	Z-Y	29 ± 29	18 ± 19	30 ± 36
		X-Y	16 ± 9	19 ± 17	21 ± 19

Another microstructural feature related to conductivity is misorientation or the grain boundary angle. Small misorientation angles (<15°) or $\sum$3-Twins ($\approx$60°) have an electric DC resistivity that is almost a factor 100 [43] or 10 [44] smaller than the random misorientations found in high angle grain boundaries. Figure 13 shows the misorientation angle distribution of the samples. Almost no $\sum$3-Twins were present in the material. Nevertheless, the misorientation angle distribution function was dominated by a high amount of small angle misorientations (<15°). It appears that annealing increased this fraction.
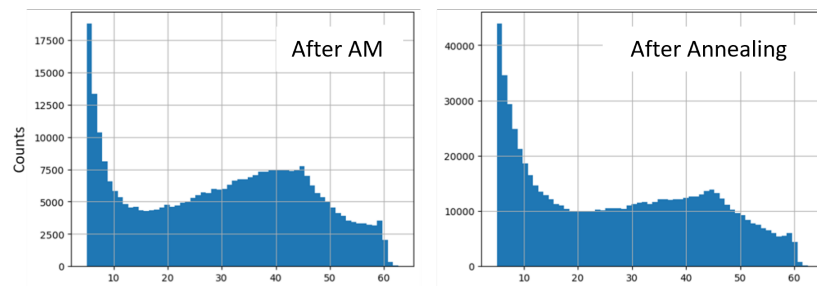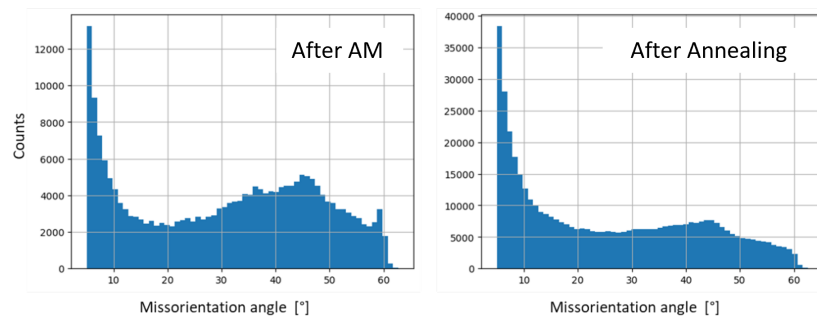

Figure 13. Misorientation angle distribution of (**a**) samples produced with red and (**b**) samples produced with green laser. After AM and after annealing.

4. Discussion

4.1. Dimensional Accuracy

We want to illustrate the measured frequency deviations by means of the deviation of the gap length g. As mentioned in Section 2.4, the conversion factor is approx. $\frac{\Delta f_R}{\Delta d} = 0.21 \frac{\text{MHz}}{\mu\text{m}}$.

After additive manufacturing: The mean values SCs R and SCs G deviated from the planned g by 3.8 μm and 19.0 μm, respectively. The maximum deviation from the planned g was 13.3 μm and 24.3 μm, respectively. To address manufacturing inaccuracies and temperature drifts, cavities are typically equipped with various frequency tuning devices

to achieve the desired f_R. Conventional tuning methods (such as tuning rods, pneumatic tuners, circumferential tuners, etc.) can achieve a maximum frequency shift Δf_R of about 4 MHz for TM_{010} cavities with an f_R of 4260 MHz, without significantly reducing the Q_0. These values were extrapolated from an analysis of the tuning characteristics of 3 GHz SCCL cells [45]. This Δf_R corresponds to a Δg of 19 μm. Especially for SCs G, the measured f_R values were higher than the planned f_R, indicating a systematic deviation related to the printing process that can be corrected iteratively. The maximum deviation from the average g of 9.5 μm and 5.2 μm for the SCs R and SCs G, respectively, lies well within the tunable range of 19 μm. Figures 5 and 6 additionally illustrate that no obvious asymmetries occurred during printing.

After post-processing: As depicted in Table 2 and Figure 8, the f_R demonstrated an increase with increasing material removal (MR). For SCs G, this yielded an average shift of the resonant frequency per unit material removal ($\frac{\Delta f}{\Delta MR}$) of approximately 0.41 $\frac{\text{MHz}}{\text{μm}}$. Conversely, for SCs R, the corresponding value for $\frac{\Delta f}{\Delta MR}$ was approximately 0.60 $\frac{\text{MHz}}{\text{μm}}$. It is noteworthy that with both laser types, the first 40 μm of material removal induced a greater frequency shift than the second 40 μm. This is attributed to the faster ablation of layers with incompletely melted powder, as they offer a larger effective surface area. Additionally, SC R4 exhibited a notably large Δf. This is likely due to significant unsymmetrical material removal around the nose cone in this cell (refer to the white arrow in Figure 6). Since the nosecone defines the f_R in the initial iteration, variations here exert a particularly pronounced effect.

Figures 5 and 6 also illustrate that the symmetry of the SCs diminished with increasing material removal (MR). As more material was removed, increased waviness became apparent (see black arrows in Figure 6), stemming from the flow direction of the post-processing media and raising gas bubbles, as previously discussed in [23]. Nevertheless, especially for low MR values, the symmetry could be greatly increased compared to [23], which is most likely due to the rotation of the SCs during the process.

4.2. Electrical Surface Conductivity

For the relationship between the actual surface conductivity σ_S and the simulated surface conductivity σ_{S0}, it holds that $\frac{\sigma_S}{\sigma_{S0}} = \frac{Q_0}{Q_{0\text{sim}}}$ (see Section 2.4).

After additive manufacturing: The averaged $\frac{\sigma_S}{\sigma_{S0}}$ of the SCs R and SCs G amounted to approximately 0.42 and 0.22, respectively, after printing (see Table 5). This reduction in σ_S compared to σ_{S0} can mainly be attributed to the high surface roughness of the SCs, which in both cases extended over several skin depths. While annealing has no effect on the SC R1, SC G1 experienced an increase in σ_S of approximately 17%. The underlying cause of this increase cannot be unequivocally inferred from the available results. We favor the idea that annealing has removed surface contaminants. A change in the grain structure appears unlikely (see Section 3.5).

After post-processing: Hirtisation® enhanced the quality of both the SCs R and SCs G. For SC R2, a surface conductivity ratio $\frac{\sigma_S}{\sigma_{S0}}$ of approximately 93% was achieved after a removal depth MR of 40 μm. SC R3 and SC R4 reached 91% and 100%, respectively. Surface roughness measurements confirmed the trend of $\frac{\sigma_S}{\sigma_{S0}}$ with increasing material removal, although for SC R3, a higher value would be expected. This trend for SCs R was maintained even after annealing, suggesting that either irregularities in the geometry induced by post-processing or the material density may influence SC R3. The printing parameters of additive manufactured components typically differ for the part's contours and its interior (hatching). In the transition zone between the contours and hatching, irregularities in the lattice and printing defects may occur more frequently. It is possible that at $MR = 100$ μm, this transition zone was more exposed, potentially leading to a decrease in the surface conductivity of SC R3 compared to SC R2, despite a simultaneous decrease in the surface roughness.

For the SCs G, the ratio $\frac{\sigma_S}{\sigma_{S0}}$ increased uniformly up to $MR = 100$ µm. The influence of the final Hirtisation® step in terms of enhancing $\frac{\sigma_S}{\sigma_{S0}}$ per µm was approximately two times lower than that of the first two steps. This suggests an approach toward the surface roughness required to achieve high surface conductivity. SC G4 achieved a $\frac{\sigma_S}{\sigma_{S0}}$ of approximately 0.85, which was about 9% less than SC R2. The $\bar{S}_{q26\mu m}$ of SC G4 was approximately 0.81 µm, which was around 19% higher than that of SC R2, thus reflecting the expected trend. It can therefore be assumed that SCs produced with green laser would achieve $\frac{\sigma_S}{\sigma_{S0}} > 0.9$ if MR were further increased.

After annealing: Annealing resulted in an increase of $\frac{\sigma_S}{\sigma_{S0}}$ for all SCs except for SC G1. For SCs processed with Hirtisation®, this increase ranged between 3% and 7%. No systematic dependence on the MR could be observed. The cause of this increase needs to be further investigated in subsequent studies. Nevertheless, some conclusions can be drawn.

The EDS measurements have shown that during Hirtisation®, CuCl was deposited on the surface of the geometries, which appearred to be either absent or significantly reduced after annealing. This result is further supported by the fact that the vapor pressure of CuCl is 1 hP at 440 °C, suggesting that it has evaporated at the annealing temperature of 460 °C. Taking into account the average analysis depth of 50 nm with EDS, as well as the ratio of Cu counts and Cl counts for the pure CuCl sample and the sample after Hiritisation, it can be assumed that the CuCl layer caused by Hiritisation® should be in the single-digit nanometer range.

The EBSD measurements, on the other hand, have shown that the grain size virtually did not increase due to annealing. Furthermore, the average grain sizes consistently remained in the range of >10 µm. Studies such as [46] suggest that grain sizes only have a significant impact on electrical conductivity in the direct current (DC) case once the average grain diameter is below approximately 400 nm. In addition, it was found out by Thomas et al. [41] that the texture of electron-beam-produced copper parts has only a little effect on the AC conductivity with a frequency of 480 kHz. Misorientation in the structure can also influence the conductivity. It appears that annealing slightly increases the amount of small angle misorientations (<15°), which may lead to an improvement in σ_S (compare Figure 13). However, to the best of the authors' knowledge, there are no studies describing the influence of grain sizes or misorientations on alternating current (AC) in the S-band frequency range.

Further studies will be carried out to assess how large the influence on Q of the individual effects actually is. Considering that the assumed CuCl layer thickness, the skin depth of about 1 µm (for copper and 4.2 GHz), and that the Q_0 was only increased by a few percent by annealing, we assume that a large proportion of the the the Q_0 increase primarily resulted from the purification of the surface from CuCl, H_2O, or CO_2.

Comparison with gradient model: The comparison between the measured Q_0 values of individual SCs and the expected quality factor Q_{0sim}, calculated using the Gradient Model for the measured $S_{q\lambda}$, reveals that the $\frac{\sigma_S}{\sigma_{S0}}$ ratio performed significantly better than expected for $\lambda_c = 26$ µm. For $\lambda_c = 14$ µm, some measured values agreed with the gradient model within the errors. Nevertheless, a systematic deviation to higher Q_0 values is recognizable.

Although this is encouraging from a performance perspective, it also indicates that after the initial positive results in [23], our model for predicting σ_S using $S_{q\lambda}$ still needs further optimization. These results show that the choice of the cutoff wavelength λ_c must be refined by further studies. In addition, the approach of applying an average roughness for the entire cavity must be reconsidered. After all, different geometry sections show slightly different roughness and in some cases very different current densities or EM field strengths.

5. Conclusions

In this work, four 4.2 GHz single cavities were fabricated using L-PBF systems based on red and green lasers. Subsequently, the single cavities were post-processed through Hirtisation® and annealing.

Both L-PBF processes achieved the necessary printing accuracy and density to produce S-band cavities for currently deployed Linac systems. To achieve the required surface conductivity for Linac applications, the surface roughness must be reduced. This was accomplished through the process of Hirtisation® and subsequent annealing, with the cavities produced using red lasers reaching σ_{S0} after a material removal of only 40 μm, while for cavities produced with green laser, more than 160 μm removal was required. The difference is mainly attributed to the initial surface roughness, which was approximately two times lower for the cavities printed with red lasers compared to those printed with green lasers. The reduced processing time or material removal compared to cavities produced with green lasers also has the advantage of practically avoiding asymmetries in the internal geometry induced by Hirtisation®.

In total, the additive manufactured cavities presented in this study encourage high-gradient tests. For the first time, the surface conductivity required for Linacs was achieved through post-processing while simultaneously preserving the geometric symmetry indispensable for high-gradient operation. Although both red and green L-PBF are applicable and fulfill the quality requirements, the red L-PBF resulted in even better Q values and precision in structure geometry while requiring less post-processing time.

References

1. Witman, S. Ten Things You Might Not Know about Particle Accelerators. *Symmetry Magazine*, 15 April 2014.
2. Wangler, T.P. *RF Linear Accelerators*; John Wiley & Sons: Hoboken, NJ, USA, 2008.
3. Kutsaev, S. Advanced technologies for applied particle accelerators and examples of their use. *Tech. Phys.* **2021**, *66*, 161–195. [CrossRef]
4. Lung, H.M.; Cheng, Y.C.; Chang, Y.H.; Huang, H.W.; Yang, B.B.; Wang, C.Y. Microbial decontamination of food by electron beam irradiation. *Trends Food Sci. Technol.* **2015**, *44*, 66–78. [CrossRef]
5. Do Huh, H.; Kim, S. History of radiation therapy technology. *Prog. Med Phys.* **2020**, *31*, 124–134. [CrossRef]
6. Wilson, I.H. Cavity construction techniques. In Proceedings of the CERN Accelerator School of RF Engineering for Particle Accelerators, Oxford, UK, 3–10 April 1991; Volume 2. [CrossRef]
7. Nassiri, A.; Chase, B.; Craievich, P.; Fabris, A.; Frischholz, H.; Jacob, J.; Jensen, E.; Jensen, M.; Kustom, R.; Pasquinelli, R. History and technology developments of radio frequency (RF) systems for particle accelerators. *IEEE Trans. Nucl. Sci.* **2015**, *63*, 707–750. [CrossRef]
8. Pagani, C.; Bellomo, G.; Pierini, P. A high current proton linac with 352 MHz SC cavities. *arXiv* **1996**, arXiv:acc-phys/9609004.

9. Mickat, S.; Barth, W.; Clemente, G.; Groening, L.; Schlitt, B.; Ratzinger, U. The Status of the High-Energy Linac Project at GSI. *GSI Sci. Rep.* **2014**, 306.
10. Brinkmann, R.; Andruszkow, J.; Agababyan, A.; Ageyev, A.; Andruszkow, J.; Antoine, C.; Aseev, V.; Aune, B.; Ayvazyan, V.; Baboi, N.; et al. *TESLA Technical Design Report—PART II The Accelerator*; DESY: Hamburg, Germany, 2001. Available online: https://tesla.desy.de/ (accessed on 1 December 2023).
11. Calignano, F.; Manfredi, D.; Ambrosio, E.P.; Biamino, S.; Lombardi, M.; Atzeni, E.; Salmi, A.; Minetola, P.; Iuliano, L.; Fino, P. Overview on additive manufacturing technologies. *Proc. IEEE* **2017**, *105*, 593–612. [CrossRef]
12. Sefene, E.M. State-of-the-art of selective laser melting process: A comprehensive review. *J. Manuf. Syst.* **2022**, *63*, 250–274. [CrossRef]
13. Shahrubudin, N.; Lee, T.C.; Ramlan, R. An overview on 3D printing technology: Technological, materials, and applications. *Procedia Manuf.* **2019**, *35*, 1286–1296. [CrossRef]
14. Ikeshoji, T.T.; Nakamura, K.; Yonehara, M.; Imai, K.; Kyogoku, H. Selective laser melting of pure copper. *Jom* **2018**, *70*, 396–400. [CrossRef]
15. Tran, T.Q.; Chinnappan, A.; Lee, J.K.Y.; Loc, N.H.; Tran, L.T.; Wang, G.; Kumar, V.V.; Jayathilaka, W.; Ji, D.; Doddamani, M.; et al. 3D printing of highly pure copper. *Metals* **2019**, *9*, 756. [CrossRef]
16. Hähnel, H.; Ates, A.; Ratzinger, U. Update on the first 3D printed IH-type linac structure-proof-of-concept for additive manufacturing of linac rf cavities. In Proceedings of the 31st Linear Accelerator Conference (LINAC), Liverpool, UK, 8 August–2 September 2022; Volume 31, pp. 170–173.
17. Hähnel, H.; Ateş, A.; Dedić, B.; Ratzinger, U. Additive Manufacturing of an IH-Type Linac Structure from Stainless Steel and Pure Copper. *Instruments* **2023**, *7*, 22. [CrossRef]
18. Torims, T.; Cherif, A.; Delerue, N.; Pedretti, M.F.; Krogere, D.; Otto, T.; Pikurs, G.; Pozzi, M.; Ratkus, A.; Thielmann, M.; et al. Evaluation of geometrical precision and surface roughness quality for the additively manufactured radio frequency quadrupole prototype. In *Proceedings of the Journal of Physics: Conference Series*; IOP Publishing: Bristol, UK, 2023; Volume 2420, p. 012089.
19. Torims, T.; Pikurs, G.; Gruber, S.; Vretenar, M.; Ratkus, A.; Vedani, M.; López, E.; Brückner, F. First proof-of-concept prototype of an additive manufactured radio frequency quadrupole. *Instruments* **2021**, *5*, 35. [CrossRef]
20. Riensche, A.; Carriere, P.; Smoqi, Z.; Menendez, A.; Frigola, P.; Kutsaev, S.; Araujo, A.; Matavalam, N.G.; Rao, P. Application of hybrid laser powder bed fusion additive manufacturing to microwave radio frequency quarter wave cavity resonators. *Int. J. Adv. Manuf. Technol.* **2023**, *124*, 619–632. [CrossRef]
21. Mayerhofer, M.; Mitteneder, J.; Dollinger, G. A 3D printed pure copper drift tube linac prototype. *Rev. Sci. Instruments* **2022**, *93*, 023304. [CrossRef] [PubMed]
22. Mayerhofer, M.; Mitteneder, J.; Witting, C.; Prestes, I.; Jaegle, R.; Dollinger, G. First High Quality Drift Tube Linac Cavity additively Manufactured from Pure Copper. In Proceedings of the 14th International Particle Accelerator Conference, Venice, Italy, 7–12 May 2023; Volume 23.
23. Mayerhofer, M.; Brenner, S.; Helm, R.; Gruber, S.; Lopez, E.; Stepien, L.; Gold, G.; Dollinger, G. Additive Manufacturing of Side-Coupled Cavity Linac Structures from Pure Copper: A First Concept. *Instruments* **2023**, *7*, 56. [CrossRef]
24. Ratkus, A.; Rarison, S.; Garion, C.; Kos, H.; Gruber, S.; Stepien, L.; Patil, A.; Lopez, E.; Torims, T.; Pikurs, G.; et al. Evaluation of green laser source additive manufacturing technology for accelerator applications with ultra-high vacuum requirements. In *Proceedings of the Journal of Physics: Conference Series*; IOP Publishing: Bristol, UK, 2024; Volume 2687, p. 082046.
25. Mayerhofer, M.; Brenner, S.; Doppler, M.; Catarino, L.; Girst, S.; Nedeljkovic-Groha, V.; Dollinger, G. Improving Fabrication and Performance of Additively Manufactured RF Cavities by Employing Co-Printed Support Structures and Their Subsequent Removal. *Instruments* **2024**, *8*, 18. [CrossRef]
26. Ratkus, A.; Torims, T.; Pikurs, G.; Bjelland, V.; Calatroni, S.; Peacock, R.; Serafim, C.; Vretenar, M.; Wuensch, W.; Vedani, M.; et al. Initial high electric field—Vacuum arc breakdown test results for additively manufactured pure copper electrodes. In Proceedings of the 14th International Particle Accelerator Conference, Venice, Italy, 7–12 May 2023; Volume 14.
27. Townsend, A.; Senin, N.; Blunt, L.; Leach, R.; Taylor, J. Surface texture metrology for metal additive manufacturing: A review. *Precis. Eng.* **2016**, *46*, 34–47. [CrossRef]
28. Punzel, E.; Hugger, F.; Dörringer, R.; Dinkelbach, T.L.; Bürger, A. Comparison of different system technologies for continuous-wave laser beam welding of copper. *Procedia CIRP* **2020**, *94*, 587–591. [CrossRef]
29. Qu, S.; Ding, J.; Fu, J.; Fu, M.; Zhang, B.; Song, X. High-precision laser powder bed fusion processing of pure copper. *Addit. Manuf.* **2021**, *48*, 102417. [CrossRef]
30. De Terris, T.; Baffie, T.; Ribiere, C. Additive manufacturing of pure copper: A review and comparison of physical, microstructural, and mechanical properties of samples manufactured with Laser-Powder Bed Fusion (L-PBF), Electron Beam Melting (EBM) and Metal Fused Deposition Modelling (MFDM) technologies. *Int. J. Mater. Form.* **2023**, *16*, 32.
31. Gruber, S.; Stepien, L.; López, E.; Brueckner, F.; Leyens, C. Physical and geometrical properties of additively manufactured pure copper samples using a green laser source. *Materials* **2021**, *14*, 3642. [CrossRef] [PubMed]
32. Yang, G.; Li, H.; Li, Z.; Zhu, Z.; Liu, R.; Zhang, Q.; Liu, Y.; Yao, J. Support design of overhanging structure for laser powder bed fusion. *J. Mater. Res. Technol.* **2023**, *24*, 8693–8702. [CrossRef]
33. Dassault Systèmes. *CST Microwave Studio*; CST Studio Suite: Houston, TX, USA, 2008.

34. Electro Optical Systems (EOS GmbH), EOS Copper CuCP. 2024. Available online: https://store.eos.info/products/eos-copper-cucp (accessed on 13 April 2024).
35. RENA Technologies Austria GmbH, Homepage. 2024. Available online: https://www.rena.com/en/company/rena-austria (accessed on 13 April 2024).
36. Herrero Martin, A.; Garcia-Verdugo Zuil, A. Additive Manufacturing and Radio Frequency Filters: A Case Study on 3D-Printing Processes, Postprocessing and Silver Coating Methods. Master's Thesis, Kungliga Tekniska Högskolan, Stockholm, Sweden, 2020.
37. *DIN EN ISO 25178-2: 2012-09*; Geometrical Product Specifications (GPS)—Surface Texture: Areal—Part 2: Terms, Definitions and Surface Texture Parameters (ISO 25178-2: 2012). European Committee for Standardization: Brussels, Belgium, 2012.
38. Gold, G.; Helmreich, K. A physical surface roughness model and its applications. *IEEE Trans. Microw. Theory Tech.* **2017**, *65*, 3720–3732. [CrossRef]
39. Soda, H.; McLean, A.; Wang, Z.; Motoyasu, G. Pilot-scale casting of single-crystal copper wires by the Ohno continuous casting process. *J. Mater. Sci.* **1995**, *30*, 5438–5448. [CrossRef]
40. Thomas, A.; Fribourg, G.; Blandin, J.J.; Lhuissier, P.; Dendievel, R.; Martin, G. Tailoring the crystallographic texture of pure copper through control of the scanning strategy in Electron Powder Bed Fusion. *Materialia* **2022**, *24*, 101495. [CrossRef]
41. Thomas, A.; Fribourg, G.; Blandin, J.J.; Lhuissier, P.; Dendievel, R.; Martin, G. Effect of the build orientation on mechanical and electrical properties of pure Cu fabricated by E-PBF. *Addit. Manuf.* **2021**, *48*, 102393. [CrossRef]
42. Jadhav, S.D.; Dadbakhsh, S.; Goossens, L.; Kruth, J.; Van Humbeeck, J.; Vanmeensel, K. Influence of selective laser melting process parameters on texture evolution in pure copper. *J. Mater. Process. Technol.* **2019**, *270*, 47–58. [CrossRef]
43. Bishara, H.; Lee, S.; Brink, T.; Ghidelli, M.; Dehm, G. Understanding grain boundary electrical resistivity in Cu: The effect of boundary structure. *ACS Nano* **2021**, *15*, 16607–16615. [CrossRef] [PubMed]
44. César, M.; Liu, D.; Gall, D.; Guo, H. Calculated resistances of single grain boundaries in copper. *Phys. Rev. Appl.* **2014**, *2*, 044007. [CrossRef]
45. Verdú Andrés, S. High-Gradient Accelerating Structure Studies and Their Application in Hadrontherapy. Ph.D. Thesis, CSIC-UV-Instituto de Física Corpuscular (IFIC), Valencia, Spain, 2013.
46. Bakonyi, I. Accounting for the resistivity contribution of grain boundaries in metals: Critical analysis of reported experimental and theoretical data for Ni and Cu. *Eur. Phys. J. Plus* **2021**, *136*, 410. [CrossRef]